JPhys Photonics

PURPOSE-LED PUBLISHING™

PAPER • OPEN ACCESS

The R-index: a universal metric for evaluating OAM content and mode purity in optical fields

To cite this article: Monika Bahl *et al* 2026 *J. Phys. Photonics* **8** 015071

View the article online for updates and enhancements.

You may also like

- Antiresonant hollow-core fiber with rapid gas exchange for mid-infrared gas spectroscopy
Mateusz Winkowski, Rafa Kasztelanic, Dariusz Pysz et al.
- Nanoscale interactions of *Salmonella typhimurium* on ZnO nanowires biosensing interfaces
Karla Paola Sanchez Roldan, Rafael A Salinas Dominguez, Shirlley E Martínez Tolibia et al.
- Taj Mahal conservation and the scope of electromagnetic sensing
Aparajita Bandyopadhyay, Puspita Chanda, Uzair Aalam et al.

This content was downloaded from IP address 81.223.14.210 on 23/03/2026 at 13:16

Journal of Physics: Photonics

Check for updates

OPEN ACCESS

RECEIVED
14 August 2025

REVISED
29 December 2025

ACCEPTED FOR PUBLICATION
7 January 2026

PUBLISHED
10 March 2026

Original content from this work may be used under the terms of the Creative Commons Attribution 4.0 licence.

Any further distribution of this work must maintain attribution to the author(s) and the title of the work, journal citation and DOI.

PAPER

The R-index: a universal metric for evaluating OAM content and mode purity in optical fields

Monika Bahl[1,*], Georgios M Koutentakis[2,*], Mikhail Maslov[2], Tom Jungnickel[1], Timo Gaßen[1], Mikhail Lemeshko[2] and Oliver H Heckl[1,*]

[1] Optical Metrology Group, Faculty of Physics, University of Vienna, Boltzmanngasse 5, 1090 Vienna, Austria
[2] Institute of Science and Technology Austria (ISTA), Am Campus 1, 3400 Klosterneuburg, Austria
[*] Authors to whom any correspondence should be addressed.

E-mail: monika.bahl@univie.ac.at, georgios.koutentakis@ist.ac.at and oliver.heckl@univie.ac.at

Keywords: structured light, optical vortex, orbital angular momentum, mode purity

Abstract

Despite its pivotal role in optical manipulation, high capacity communications, and quantum information, a general measure of orbital angular momentum (OAM) in structured light remains elusive. In optical fields, where multiple vortices coexist, the local nature of vortex OAM and the absence of a common rotation axis make the total OAM of the field difficult to quantify. Here, we introduce the R index—a metric that captures the intrinsic OAM content of any structured optical field, from pure Laguerre–Gaussian modes to arbitrary multi vortex superpositions. Not only does this metric quantify the total OAM, it also assesses field purity, providing insight into the fidelity and robustness of the OAM generation. By unifying OAM characterization into a single figure of merit, the R index enables direct comparison across diverse beam profiles and facilitates the identification of optimal configurations for both foundational studies and applied technologies.

1. Introduction

Since the seminal work of Allen *et al* [1], which demonstrated that electromagnetic waves can carry well defined orbital angular momentum (OAM), this discrete, and in principle unbounded, property of light has evolved from a theoretical concept into a practical resource. The ladder of OAM eigenstates offers high dimensional encoding capacity for classical and quantum communication [2–4], facilitates the transfer of rotational torque in optical micromanipulation [5, 6], and underpins emerging OAM-enhanced spectroscopic techniques [7]. Recent advances in wavefront-shaping optics, spiral phase plates, computer generated holograms, and spatial light modulators (SLMs), now permit the routine generation and analysis of OAM beams [8–12], thereby broadening their applicability across photonics and related disciplines [13–16], also including quantum information processing [17], particle manipulation [18], and light–matter interaction [14, 19–21].

The total angular momentum of an optical beam comprises an *intrinsic* component, determined solely by the internal field distribution, and an *extrinsic* component that depends on the displacement of the beam axis relative to the observation axis. Within the intrinsic part, one distinguishes spin angular momentum (SAM), related to the polarization of light, and OAM, which stems predominantly from the *optical vortices* [1]. In a coherent light wave, represented by a complex scalar field propagating in free space, optical vortices arise at points of zero intensity, called nodes, where the phase is undefined. Around these singularities, the phase gradient forms a circulating pattern, characterized by an azimuthal phase dependence of the form $\exp(il\phi)$, where l is the topological charge and ϕ is the azimuthal angle. Such a phase structure in an optical vortex corresponds to a quantized angular momentum of magnitude $l\hbar$ per photon. As clarified in reference [22], the helical phase factor $\exp(il\phi)$ is the principal descriptor of the intrinsic OAM. It gives rise to a precession of the Poynting vector and the associated azimuthal orbital flow density (OFD). In contrast, SAM arises from the rotation of electric field vectors and is quantified by the spin flow density (SFD) [23]. Together, OFD and SFD exhaust the intrinsic angular

© 2026 The Author(s). Published by IOP Publishing Ltd

momentum content of an optical beam. These complementary flow densities offer experimentally accessible measures of the respective angular momentum contributions.

For an ideal paraxial beam containing a single vortex, all photons share the same helical phase factor, and the OAM can be unambiguously defined with respect to the common propagation axis. But, in practice, many beams are spatially structured optical fields (SSOFs) that contain multiple vortices. In such cases, three considerations preclude a straightforward definition of the total OAM:

1. *Local character of a vortex OAM.* Each vortex is associated with a unique phase singularity ,whose topological charge may differ from charges of other vortices. The associated OAM remains local to the singularity and does not extend globally on the beam.
2. *Vortex interference.* Superposition of individual vortex wavefronts generates intricate interference patterns and secondary phase singularities, such that a simple sum of single vortex OAM does not describe the composite field.
3. *Absence of a common rotation axis.* Whereas a single vortex beam, such as a Laguerre–Gaussian (LG) mode, has a single optical axis, the vortex array in a generic SSOF is described by several, in general different, rotational axes. Subsequently, the overall field lacks global rotational symmetry.

Collectively, these factors imply that the total OAM content of an elaborately structured field cannot be deduced by enumerating vortices or by projecting onto a standard mode basis. Accessing the fitness of the field for applications, for instance, OAM enhanced spectroscopy [7] requires a quantitative measure of the rotational energy flux in terms of a more rigorous metric.

In this paper, we introduce a unified measure, the R-index, based on the relative amplitude of the solenoidal component of the OFD, which provides an estimate of the photon fraction available for OAM mediated interactions. Our calculations demonstrate its efficacy in identifying the OAM content across a broad range of beam types, including LG, Gaussians, superpositions of Hermite–Gaussian (HG) beams and vortex-bearing optical lattices making it a universal tool for structured light analysis. The ability of the R-index to reduce the OAM content characterization to a single figure-of-merit makes it an attractive tool for selecting the appropriate structure of the electric field for OAM-enabled fundamental studies or technological applications. Moreover, we demonstrate its ability to act as a quality factor by assessing the mode purity of LG modes generated by spiral phase plates. This application is particularly important for mid-infrared (Mid-IR) applications where high-fidelity optical vortex generating apparatuses, such as SLMs are unavailable.

Beam purity is an important aspect of analysis, as it helps determine the most suitable beam profile for a given application. Previous studies on modal decomposition have shown that higher-order beams often contain components of various topological charges [24], an observation that is particularly relevant for optical communication systems employing OAM multiplexing. In this work, we evaluate beam purity based on the phase distribution, quantifying the fraction of photons that are converted into states carrying OAM. While the method of beam generation or conversion may vary, the purity analysis given by the R-index, remains consistent as a given beam profile corresponds to a specific R-index. This also enables the assessment of the purity of experimentally generated beams, as imperfections that alter the OAM content will be reflected in a modified R-index when compared to the ideal case.

Our paper is structured as follows. In section 2 we review how the OFD of a light field can be extracted from its phase gradients. In section 3 we introduce our main tool the Helmholtz–Hodge decomposition (HHD), via which we can separate the solenoidal, OAM bearing, phase gradients from the irrotational part. In section 4 we define the main quantity discussed in our paper, the R-index. Section 5 summarizes the numerical techniques employed for the evaluation of the R-index. The focal parts of our work are section 6 describing our numerical findings for various field profiles and section 7 providing the analytical evaluation of the R-index for LG beams. Section 8 summarizes our findings and provides future perspectives. Finally, appendix A provides extended data tables for various superpositions of HG modes.

2. Orbital flow characteristics

Our approach consists of tracing the internal energy flows of the field, also known as optical currents, one of its intrinsic features that reveals details of its structure and dynamics [25]. These paths can be represented as curves that are everywhere tangent to the Poynting vector, a quantity that links to the dynamical attributes of optical fields. We consider a monochromatic field $\psi(\boldsymbol{r}) = |E(\boldsymbol{r})|e^{i\varphi(\boldsymbol{r})}$ and $\boldsymbol{E}(\boldsymbol{r}) = \hat{\boldsymbol{E}}_p\psi(\boldsymbol{r})$ and $\hat{\boldsymbol{E}}_p$ is the polarization of light, assumed here to be homogeneous so we can treat the electric field as scalar.

The optical current associated to the field $\psi(\boldsymbol{r})$ is $\boldsymbol{j}(\boldsymbol{r})$ [25], it equals the time-averaged energy flow and is given by

$$\boldsymbol{j}(\boldsymbol{r}) = I(\boldsymbol{r})\,\boldsymbol{\nabla}\varphi(\boldsymbol{r}), \tag{1}$$

where $I(\boldsymbol{r}) = \frac{c\epsilon_0}{2}\psi(\boldsymbol{r})\psi^*(\boldsymbol{r})$ is the intensity and $\psi^*(\boldsymbol{r})$ is the conjugate of $\psi(\boldsymbol{r})$, c represents the speed of light, ϵ_0 is the electrical permittivity of free space, $\boldsymbol{\nabla}$ represents the gradient operator, and $\varphi(\boldsymbol{r}) \equiv \arg(\psi(\boldsymbol{r}))$ is the phase of the optical field. The optical current is closely associated with the Poynting vector $\boldsymbol{P}(\boldsymbol{r})$, indicating the flow of energy and is directly proportional to the canonical energy flow density. The Poynting vector reads

$$\boldsymbol{P}(\boldsymbol{r}) = \frac{\mathrm{Im}\left[\psi^*\boldsymbol{\nabla}\psi\right]}{2\mu_0\omega} = \frac{|\psi|^2\boldsymbol{\nabla}\varphi(\boldsymbol{r})}{2\mu_0\omega} = \frac{1}{k}I(\boldsymbol{r})\,\boldsymbol{\nabla}\varphi(\boldsymbol{r})\,. \tag{2}$$

Here, μ_0 denotes the vacuum permeability, ω is the angular frequency, k is the wave vector and λ represents the wavelength of the optical field.

The right hand side of the above directly yields the relation $\boldsymbol{P}(\boldsymbol{r}) = \boldsymbol{j}(\boldsymbol{r})/k$. This expression also shows the association of both $\boldsymbol{j}(\boldsymbol{r})$ and $\boldsymbol{P}(\boldsymbol{r})$ with the the probability current in quantum mechanics $\mathrm{Im}[\psi^*(\boldsymbol{r})\boldsymbol{\nabla}\psi(\boldsymbol{r})]$ and which is sometimes used synonymously with the Poynting vector in electromagnetic fields. $\boldsymbol{P}(\boldsymbol{r})$ is essential for calculating the OAM of any optical field and aids in understanding how small particles interact with the field [26]. This momentum density has a transverse azimuthal component produced by the helical phase of the optical vortex and is a signature of the vortex modes. It is canonical and proportional to the local gradient of the phase of the field, that is, to the local wave vector. Therefore, the canonical orbital energy flow is independent of the polarization in uniformly polarized fields and can be equally defined for a scalar wave field $\psi(\boldsymbol{r})$.

As demonstrated in equations (1) and (2), both the optical current and the Poynting vector can be expressed in terms of the phase gradient, given by

$$\boldsymbol{\nabla}\varphi(\boldsymbol{r}) = \mathrm{Im}\left[\boldsymbol{\nabla}\log\psi(\boldsymbol{r})\right] = \mathrm{Im}\left[\frac{\boldsymbol{\nabla}\psi(\boldsymbol{r})}{\psi(\boldsymbol{r})}\right]. \tag{3}$$

This gradient points in the direction where there is a maximum change in phase. Gradients are normal to contour surfaces, and hence the phase gradient is always normal to the wavefront [27]. The phase gradient $\boldsymbol{\nabla}\varphi(\boldsymbol{r})$ is a vector field that can provide information about light propagation as $\boldsymbol{\nabla}\varphi(\boldsymbol{r}) \propto \boldsymbol{k}(\boldsymbol{r})$, with $\boldsymbol{k}(\boldsymbol{r})$ the local wavevector, and the associated energy flow.

We are mainly concerned with the energy flow on a plane perpendicular to the propagation axis of the beam, which dictates how a planar probe interacts with light. The associated phase gradient field reads

$$\boldsymbol{F}(\boldsymbol{r}) \equiv \boldsymbol{\nabla}\varphi(\boldsymbol{r}) - \frac{\boldsymbol{k}}{\boldsymbol{k}^2}\boldsymbol{k}\cdot\boldsymbol{\nabla}\varphi(\boldsymbol{r})\,. \tag{4}$$

By applying the HHD, discussed in section 3, we isolate the rotational energy flows or solenoidal phase gradients within the field [28], enabling us to distill the OAM content of the beam.

3. HHD

The HHD is grounded in the Helmholtz theorem [29], which asserts that any field $\boldsymbol{f}(\boldsymbol{r})$, defined in a region Ω on a bounded, simply connected domain, can be segregated into an irrotational (curl-free) $\boldsymbol{f}_{\mathrm{IR}}(\boldsymbol{r})$ and a solenoidal (divergence-free) $\boldsymbol{f}_{\mathrm{R}}(\boldsymbol{r})$ component, determined by

$$\boldsymbol{f}(\boldsymbol{r}) = \underbrace{\boldsymbol{\nabla}\Phi(\boldsymbol{r})}_{\equiv\boldsymbol{f}_{\mathrm{IR}}(\boldsymbol{r})} + \underbrace{\boldsymbol{\nabla}\times\boldsymbol{A}(\boldsymbol{r})}_{\equiv\boldsymbol{f}_{\mathrm{R}}(\boldsymbol{r})}, \tag{5}$$

where $\Phi(\boldsymbol{r})$ and $\boldsymbol{A}(\boldsymbol{r})$ are the scalar and vector potentials of $\boldsymbol{f}(\boldsymbol{r})$, respectively, not to be confused with the corresponding scalar and vector potentials of the electric and magnetic field.

An intuitive understanding of the Helmholtz–Hodge decomposition (HHD) follows by considering the vector identities

$$\begin{aligned}\boldsymbol{\nabla}\cdot(\boldsymbol{\nabla}\times\boldsymbol{A}(\boldsymbol{r})) &= 0,\\ \boldsymbol{\nabla}\times(\boldsymbol{\nabla}\Phi(\boldsymbol{r})) &= \boldsymbol{0},\end{aligned} \tag{6}$$

which hold for any vector $\boldsymbol{A}(\boldsymbol{r})$ and scalar $\Phi(\boldsymbol{r})$ field [28, 30].

Taking the divergence of equation (5) yields the Poisson equation

$$\nabla \cdot \boldsymbol{f}(\boldsymbol{r}) = \nabla^2 \Phi(\boldsymbol{r}) = \nabla \cdot \boldsymbol{f}_{\mathrm{IR}}(\boldsymbol{r}) \tag{7}$$

and therefore the divergence of a field is solely contained in the irrotational component $\boldsymbol{f}_{\mathrm{IR}}(\boldsymbol{r}) = \nabla\Phi(\boldsymbol{r})$.

Similarly, taking the curl of equation (5) gives

$$\nabla \times \boldsymbol{f}(\boldsymbol{r}) = \nabla \times (\nabla \times \boldsymbol{A}(\boldsymbol{r})) = \nabla \times \boldsymbol{f}_{\mathrm{R}}(\boldsymbol{r}) \tag{8}$$

showing that the curl structure of the field is carried only by the solenoidal part $\boldsymbol{f}_{\mathrm{R}}(\boldsymbol{r})$.

Taken together, equations (7) and (8) provide the intuitive picture that the HHD is possible exactly because the structure of a vector field in terms of divergence and curl provides information associated with different components of the field. Indeed, the divergence encodes the tendency of the field in the vicinity of a point to orient *towards* or *away from* it, while the curl encodes the tendency of the field to *circulate* around the point by orienting in a perpendicular fashion.

Equations (7) and (8) are also useful for the exact calculation of the HHD. More specifically, for a given vector field $\boldsymbol{f}(\boldsymbol{r})$, the inhomogeneous Poisson equation corresponding to the first equality of equation (7) for $\Phi(\boldsymbol{r})$ can be solved directly. Using the Green's-function method, the formal solution is

$$\Phi(\boldsymbol{r}) = -\frac{1}{4\pi}\int_V \frac{\nabla \cdot \boldsymbol{f}(\boldsymbol{r}')}{|\boldsymbol{r}-\boldsymbol{r}'|}\,\mathrm{d}V'. \tag{9}$$

The irrotational component of the field then follows immediately from its definition,

$$\boldsymbol{f}_{\mathrm{IR}}(\boldsymbol{r}) = \nabla\Phi(\boldsymbol{r}). \tag{10}$$

The solenoidal component can subsequently be obtained from equation (5) as

$$\boldsymbol{f}_{\mathrm{R}}(\boldsymbol{r}) = \boldsymbol{f}(\boldsymbol{r}) - \boldsymbol{f}_{\mathrm{IR}}(\boldsymbol{r}). \tag{11}$$

An equivalent reconstruction strategy can be formulated from equation (8) by first evaluating the curl $\nabla \times \boldsymbol{f}(\boldsymbol{r})$ and then solving a vector Poisson equation to recover $\boldsymbol{A}(\boldsymbol{r})$ (or directly $\boldsymbol{f}_{\mathrm{R}}(\boldsymbol{r})$). Within the Green's-function framework, the corresponding solution is

$$\boldsymbol{A}(\boldsymbol{r}) = \frac{1}{4\pi}\int_V \frac{\nabla \times \boldsymbol{f}(\boldsymbol{r}')}{|\boldsymbol{r}-\boldsymbol{r}'|}\,\mathrm{d}V', \tag{12}$$

where the Coulomb gauge condition $\nabla \cdot \boldsymbol{A}(\boldsymbol{r}) = 0$ has been imposed.

These potentials $\Phi(\boldsymbol{r})$ and $\boldsymbol{A}(\boldsymbol{r})$ allow the field $\boldsymbol{f}(\boldsymbol{r})$ to be segregated into the curl-free and divergence-free components within a volume V. The boundary conditions that are imposed in this decomposition ensure a normal boundary flow on the curl-free component and a tangential flow on the divergence-free component. Considering $\hat{\boldsymbol{n}}$ as the outward normal to the boundary Ω, this implies that for a unique decomposition:

- the irrotational component is normal to the boundary $\mathrm{d}\Omega$ of Ω, i.e. $\boldsymbol{f}_{IR}(\boldsymbol{r}) \times \hat{\boldsymbol{n}} = \boldsymbol{0}$, and
- the solenoidal component is parallel to the boundary $\mathrm{d}\Omega$ of Ω, i.e. $\boldsymbol{f}_{\mathrm{R}}(\boldsymbol{r}) \cdot \hat{\boldsymbol{n}} = 0$.

Under these boundary conditions the HHD is unique up to a gauge transformation of $\Phi(\boldsymbol{r})$ and $\boldsymbol{A}(\boldsymbol{r})$, that does not affect the field components $\boldsymbol{f}_{IR}(\boldsymbol{r})$ and $\boldsymbol{f}_{\mathrm{R}}(\boldsymbol{r})$.

4. Main quantities: the definition of the R-index and the solenoidal current

The R-index is defined as the fraction of the solenoidal current, $\boldsymbol{j}_{\mathrm{R}}(\boldsymbol{r}) = I(\boldsymbol{r})\boldsymbol{f}_{\mathrm{R}}(\boldsymbol{r})$, over the sum of the solenoidal and irrotational, $\boldsymbol{j}_{\mathrm{IR}}(\boldsymbol{r}) = I(\boldsymbol{r})\boldsymbol{f}_{IR}(\boldsymbol{r})$, components

$$R(z) = \frac{\iint |\boldsymbol{f}_{\mathrm{R}}(\boldsymbol{r})| I(\boldsymbol{r})\,\mathrm{d}A}{\iint (|\boldsymbol{f}_{\mathrm{R}}(\boldsymbol{r})| + |\boldsymbol{f}_{IR}(\boldsymbol{r})|) I(\boldsymbol{r})\,\mathrm{d}A}. \tag{13}$$

The intensity weight appears naturally because the optical current $\boldsymbol{j}(\boldsymbol{r})$ already contains $I(\mathbf{r})$ (cf equation (1)). Multiplying the magnitude of the solenoidal component $|\boldsymbol{f}_{\mathrm{R}}(\boldsymbol{r})|$ by $I(\boldsymbol{r})$ therefore yields the actual flow associated with that component. Consequently $R(z)$ can be interpreted as

'the fraction of the total transverse optical flow that circulates azimuthally (and hence, contributes to the OAM)'.

Since the denominator also contains the irrotational contribution, a value $R = 1$ means that 'all' of the transverse power is rotating (a pure vortex), whereas $R = 0$ means that the flow is purely radial. Intermediate values quantify the purity of the OAM mode. The weighting by $I(\mathbf{r})$ is indispensable: without it, the ratio would reduce to a simple geometric average of the magnitudes, which does not reflect the actual current enabling OAM transfer. In the remainder of this paper we show that the R-index serves as a valuable metric for determining the available intrinsic orbital flow in structured fields, offering insight into their suitability for various OAM-based applications.

It is important to note that the R-index does not quantify the absolute strength of the solenoidal current; rather, it reflects only its fraction relative to the irrotational component. Consequently, comparing two beams using the R-index alone does not allow one to infer which beam possesses a larger solenoidal current amplitude. To address this limitation, we additionally compute a normalized measure of the solenoidal current strength in our analysis,

$$\bar{J}_{\mathrm{s}}(z) = \frac{\iint |\boldsymbol{f}_{\mathrm{R}}(\boldsymbol{r})| I(\boldsymbol{r})\ \mathrm{d}A}{\iint I(\boldsymbol{r})\ \mathrm{d}A}, \tag{14}$$

which directly probes the amplitude of the solenoidal currents in the beam. It should be noted that this quantity is not dimensionless; instead, it scales inversely with the characteristic length scale of the field's spatial structure. For beams, one has $\bar{J}_{\mathrm{s}} \propto w_0^{-1}$, where w_0 is the beam width parameter, indicating that tighter beams exhibit stronger currents due to the larger associated phase gradients, equation (1).

5. Numerical approach

The HHD of the phase gradient vector field was carried out by employing fast Fourier transform (FFT) techniques. The field $\boldsymbol{F}(\boldsymbol{r})$ was first sampled on a uniform Cartesian grid by employing equations (3) and (4) for its extraction from $\psi(\boldsymbol{r})$ and its on-plane projection respectively. The grid was chosen such as it corresponds to a FFT discrete variable representation (DVR) [31] enabling the efficient calculation of derivatives and integrals. Since FFT introduces periodic boundary conditions the value of $\psi(\boldsymbol{r})$ at the edges of our numerical grid were masked by Tukey windows to avoid artifacts. Notice that the mask of the Tukey windows addresses only regions of $I < 10^{-6} I_0$, which are subsequently dropped from our analysis.

The HHD was performed by numerically solving the Poisson equation

$$\nabla^2 \Phi(\boldsymbol{r}) = \boldsymbol{\nabla} \cdot \boldsymbol{f}(\boldsymbol{r}), \tag{15}$$

This equation can be solved by calculating $\Phi(\boldsymbol{r})$ using equation (9). The individual components are calculated by using $\boldsymbol{f}_{\mathrm{IR}}(\boldsymbol{r}) = \boldsymbol{\nabla}\Phi(\boldsymbol{r})$ and $\boldsymbol{f}_{\mathrm{R}}(\boldsymbol{r}) = \boldsymbol{F}(\boldsymbol{r}) - \boldsymbol{\nabla}\Phi(\boldsymbol{r})$ as described in section 3. The right hand side $\boldsymbol{\nabla} \cdot \boldsymbol{f}(\boldsymbol{r})$ can exhibit steep behavior close to the vortices, we resort to a FFT-based finite difference solver for the Poisson equation [32] in order to avoid issues with spectral ringing. Within this approach the solution in Fourier space reads

$$\mathcal{F}[\Phi](k_x, k_y) = \frac{1}{2}\left(\frac{\cos\frac{2\pi k_x}{N_x} - 1}{\Delta x^2} + \frac{\cos\frac{2\pi k_y}{N_y} - 1}{\Delta y^2}\right)^{-1} \mathcal{F}[\boldsymbol{\nabla} \cdot \boldsymbol{f}](k_x, k_y), \tag{16}$$

where k_μ, N_μ, $\Delta\mu$, with $\mu = \{x, y\}$ are the grid positions, number of grid points, grid spacing for the μ direction respectively and $\mathcal{F}$ represents the FFT. The boundary condition $\boldsymbol{f}_{\mathrm{IR}}(\boldsymbol{r}) \times \hat{\boldsymbol{n}} = \boldsymbol{0}$ is enforced geometrically by the mirror symmetry of the source $\boldsymbol{\nabla} \cdot \boldsymbol{f}(\boldsymbol{r})$ for $x \to -x$ and $y \to -y$ that we impose by appropriately choosing the orientation of the beam $\psi(\boldsymbol{r})$ and the periodic boundary conditions naturally stemming from the FFT.

All calculations were performed in MATLAB. The FFT-based DVR employed 4096 points in each spatial direction and extended over the region $|x|, |y| < 4\sqrt{o} w_0$, where $o \geqslant 1$ denotes the maximum mode order of the LG or HG components. Tukey windows were applied to taper the outer 20% of the grid. The above choices provide sufficient resolution to capture both the fine structure of the field and allow for the smooth decay towards the boundaries.

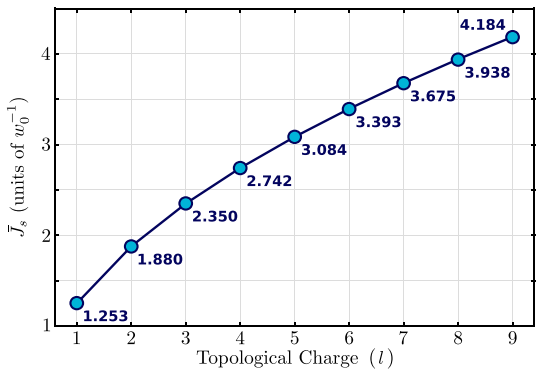

Figure 1. The normalized solenoidal current strength, $\bar{J}_s$, as a function of the topological charge for LG beams ($p = 0$ and $l = 1$–9) for $z = 0$.

6. Results: evaluation of R-index across various field profiles

We conducted extensive numerical calculations to compute the R-index for diverse SSOF profiles, demonstrating its universal applicability in quantifying the OAM content. This quantity, defined as the intensity-weighted fraction of solenoidal optical currents, equation (13), serves as a direct metric for OAM accessibility in photons. To quantify the solenoidal field flow we also evaluate the normalized solenoidal current strength, $\bar{J}_s$, see equation (14).

Throughout our analysis we use scaled units with respect to w_0 and z_R. Since we consider fixed z/z_R, the precise value of λ for fixed w_0 does not affect our calculations except for a shift of the phase $\sim e^{-ikz}$, that affects neither $\bar{J}_s$ or the R-index.

Our key findings are summarized below:

Pure LG beams—the profile of these beams reads

$$\psi_{p,l}^{\mathrm{LG}}(\boldsymbol{r}) = E_0 \frac{w_0}{w(z)} \left(\frac{\sqrt{2}r}{w(z)}\right)^{|l|} L_p^{|l|}\left(\frac{2r^2}{w(z)^2}\right) \exp\left(-\frac{r^2}{w(z)^2}\right) \exp\left(-\mathrm{i}\frac{kr^2}{2\mathcal{R}(z)}\right) \times \exp(-\mathrm{i}kz) \exp(\mathrm{i}\xi(z)) \exp(\mathrm{i}l\phi), \tag{17}$$

where E_0 is the field amplitude, w_0 the beam waist, $w(z) = w_0\sqrt{1+(z/z_R)^2}$, $z_R = \pi w_0^2/\lambda$ is the Rayleigh range, $\mathcal{R}(z) = z[1+(z_R/z)^2]$ is the radius of curvature, and $\xi(z) = (|l|+p+1)\tan^{-1}(z/z_R)$ is the Gouy phase.

Exactly at the focus $z = 0$, these beams have a purely azimuthal $\boldsymbol{F}(\boldsymbol{r})$, leading to a purely solenoidal current since $\boldsymbol{\nabla}\cdot\boldsymbol{f}(\boldsymbol{r}) = 0$, and hence an R-index of 1. The strength of this solenoidal current increases with the topological charge $\bar{J}_s \sim \sqrt{2l}$ as revealed in figure 1. However, as the beam propagates away from its focus its divergence leads to additional radial currents that cause the reduction of the R-index. Details on the z/z_R dependence of the R-index for LG beams are discussed in section 7. For comparison to other field profiles, here, we consider a beam propagated to $z = 0.1\ z_R$. Table 1 reveals that such a beam with $p = 0$ and $l = 1$ achieves an R-index of 0.87 thus retaining near-ideal OAM purity (87% rotational energy flow).

The fraction of solenoidal orbital optical current density values were computed for LG beams with varying topological charges, revealing the increasing relationship (see table 2 and figure 1).

Phase imprinted Gaussian beam (Hypergeometric Gaussian (HyGG) beams)—a common method for experimentally generating vortex beams is by imprinting the azimuthal phase of a LG mode onto a Gaussian beam. This is because Gaussian modes can be generated with very high fidelity [33, 34] and phase imprinting can be achieved with readily available methods such as spiral phase plates or SLMs [35]. To consider such a phase imprinting process, we examine the ideal case of a focused Gaussian beam with an additional spiral phase corresponding to $l = 1$

$$\psi^{\mathrm{IM}}(r,\phi,z=0) = E_0 \exp\left(-\frac{r^2}{w_0^2}\right) e^{\mathrm{i}\phi}. \tag{18}$$

Table 1. Numerically obtained OAM content characteristics for three example SSOF profiles. The OAM is characterized in terms of the R-index and $\bar{J}_s$ and the corresponding intensity pattern (the phase appears in the inset) is additionally provided. For the comparison of the beam and lattice $\bar{J}_s$ and phase $\lambda = 0.0035 w_0$ is considered.

SSOF profile	Pure LG beam ($l = 1$ and $z = 0.1\,z_R$)	Gaussian beam =with imprinted LG phase ($l = 1$ and $z = 0.1\,z_R$)	Honeycomb optical lattice
$\bar{J}_s/w_0^{-1}$	1.247	1.856	27.95 ($0.0978\,\lambda^{-1}$)
R-index	0.87	0.11	0.70
Intensity profile of SSOF	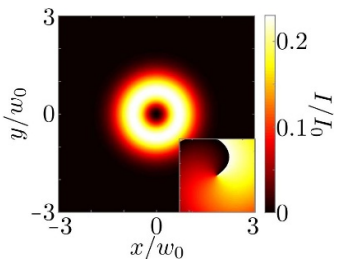	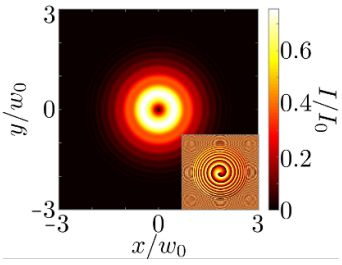	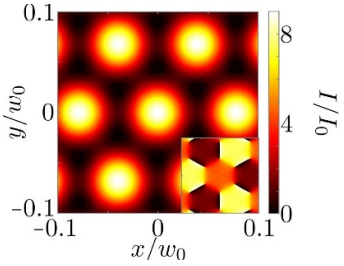

Table 2. Magnitude of extracted solenoidal phase gradient $\bar{J}_s$ and R-index for pure LG beams (topological charges 1–9) at $z = 0.1 z_R$ from focus.

Topological Charge l	$\bar{J}_s$ units of w_0^{-1}	R-index
1	1.247	0.869
2	1.871	0.889
3	2.338	0.896
4	2.728	0.899
5	3.069	0.901
6	3.376	0.902
7	3.657	0.903
8	3.918	0.904
9	4.163	0.905

The solution of the paraxial equation with the above field at the focus $z = 0$ is known to be an example of a HyGG mode and in particular a modified Bessel–Gauss mode [36]. The field of this beam reads

$$\psi^{\mathrm{IM}}(\tilde{r},\phi,\tilde{z}) = E_0 \frac{\sqrt{\pi}}{2} \frac{\tilde{r}}{\sqrt{\tilde{z}(\tilde{z}+i)}^{3/2}} \exp\left(-\frac{\mathrm{i}\tilde{r}^2}{\tilde{z}}\right) \left[I_0\left(\frac{\tilde{r}^2}{2\tilde{z}(\tilde{z}+i)}\right) - I_1\left(\frac{\tilde{r}^2}{2\tilde{z}(\tilde{z}+i)}\right)\right] \times \exp\left(-\frac{\tilde{r}^2}{2\tilde{z}(\tilde{z}+i)} + \mathrm{i}\phi - \mathrm{i}kz\right), \tag{19}$$

where we have introduced the scaled coordinates $\tilde{z} = z/z_R$ and $\tilde{r} = r/w_0$. A distinctive property of this beam is the factor $\mathrm{e}^{-\mathrm{i}\tilde{r}^2/\tilde{z}}$ corresponding to a steep phase gradient in the direction away from the focus. This gradient correspond to a radial current $\boldsymbol{j}(\boldsymbol{r})$ that forces the intensity away from $r = 0$ where the optical vortex is imprinted.

Table 1 manifests that while the solenoidal current $\bar{J}_s$ is similar in amplitude to the case of the vortex beam, the R-index is very small taking a value of 0.11. This behavior occurs exactly because of the large radial current described above which contributes to the irrotational part of the phase gradient, $\boldsymbol{F}_{\mathrm{IR}}(\boldsymbol{r})$.

The above shows that the R-index is a sensitive probe of the purity of the generated OAM mode. By quantifying SPP-generated beam purity, the R-index provides a tool for optical vortex generation protocols. Its measurement by state-of-the-art phase measurement approaches such as phase-shifting holography [37], provides a detection pathway for optimizing fabrication tolerances of optical elements and alignment protocols. This is particularly crucial for Mid-IR applications where SLMs are unavailable necessitating the development of novel optical vortex creation techniques.

Honeycomb optical lattice—an interference of three plane waves produces an optical vortex lattice, the field profile of which reads

$$\psi^{\mathrm{L}}(\boldsymbol{r}) = E_0 \sum_{j=1}^{3} \exp\left[-\mathrm{i}k\left(\sin\theta\cos\phi_j x + \sin\theta\sin\phi_j y + \cos\theta z\right)\right], \tag{20}$$

where $k = 2\pi/\lambda$, $\theta = 1.7°$ is the angle of the plane-waves with respect to z-axis, and ϕ_j are the corresponding azimuthal angles ($\phi_1 = 120°$, $\phi_2 = 240°$, $\phi_3 = 360°$).

Table 3. Comparison of different SSOFs generated by superpositions of Hermite–Gaussian modes. The OAM is characterized in terms of the R-index and $\bar{J}_s$ and the corresponding intensity pattern (and phase in the case of phase imprinted Gaussian profile) is additionally provided. In all cases the field at the focus $z = 0$ is considered.

SSOF profile	$HG_{2,0} + HG_{0,2}$	$HG_{2,0} + HG_{0,2}$	$HG_{1,3} + HG_{3,1}$
Phase difference	$\pi/2$	$\pi/4$	$\pi/2$
$\bar{J}_s/w_0^{-1}$	1.410	1.383	1.653
R-index	0.74	0.66	0.83
Intensity profile	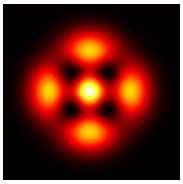	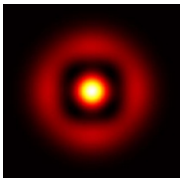	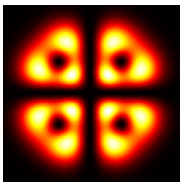

This lattices exhibits an R-index of 0.70, when measured in the $z = 0$ plane, see table 1. This structure yields a large local solenoidal current as indicated by $\bar{J}_s$, but fragmentation of dark cores leads to low percentage of OAM content. Notice that in the case of the lattice $\bar{J}_s$ is only dependent on λ. Here the value of $\bar{J}_s$ in terms of $w_0^{-1} = 0.0035\lambda^{-1}$ is provided for comparison of the lattice and beam currents.

HG superpositions—HG beams of order m, n, $HG_{m,n}$, are described by the well-known expression:

$$\psi_{m,n}^{\mathrm{HG}}(\boldsymbol{r}) = E_0 \frac{w_0}{w(z)} H_m\left(\frac{\sqrt{2}x}{w(z)}\right) H_n\left(\frac{\sqrt{2}y}{w(z)}\right) \exp\left(-\frac{x^2+y^2}{w(z)^2}\right) \exp\left(-\mathrm{i}k\frac{x^2+y^2}{2\mathcal{R}(z)}\right) \times \exp\left(-\mathrm{i}\xi(z)\right) \exp\left(-\mathrm{i}kz\right). \tag{21}$$

where H_m and H_n are Hermite polynomials of orders m and n, and $w(z)$, $\mathcal{R}(z)$, and $\xi(z) = (m + n + 1)\tan^{-1}(z/z_{\mathrm{R}})$ denote the beam radius, radius of curvature, and Gouy phase, respectively. The expressions for $w(z)$ and $R(z)$ are identical to the case of LG beams, see equation (17).

Complex modes exhibiting optical vortices are formed by superpositions of such HG modes [38, 39] with varied phase differences introduced between them.

HG superposed profiles showed reduced R-index values, underscoring mode interference as a critical purity-limiting factor. It is evident that the phase difference between superposed modes significantly influences the R-index, as anticipated. For example, table 3 shows that a superposition of $HG_{2,0}$ and $HG_{0,2}$ modes with a phase difference of $\pi/2$ yields an R-index of 0.74, which decreases to 0.66 when the phase difference is modified to $\pi/4$. In comparison, a superposition of $HG_{1,3}$ and $HG_{3,1}$ modes with a phase difference of $\pi/2$ achieves an R-index of 0.83, indicating that nearly 83% of the photons in this configuration are available for OAM-based experimental applications.

Table 4 in appendix presents R-index values for a more diverse collection of structurally singular optical fields formed through HG mode superpositions.

Our analysis demonstrates that LG beams are optimal for efficient OAM transfer to planar targets. However, realizing high-purity LG beams necessitates the use of high-fidelity beam generation, which can be challenging, particularly in the Mid-IR spectral range. Given the absence of SLMs in the Mid-IR and the current limitations in continuous SPP fabrication, it may be advantageous in some cases to employ superpositions of HG modes or structured alternatives like vortex arrays which become viable substitutes, as they achieve comparable intrinsic OAM densities despite variations in spatial profiles and mode compositions. For instance, consider the $HG_{3,1} + HG_{1,3}$ $(\pi/2)$ superposition, with an R-index of 0.83. This finding is particularly relevant to our intended application in Mid-IR OAM-enhanced spectroscopy, which fundamentally depends on phase gradient driven effects [7]. Our industrial collaborators have confirmed that phase plates corresponding to the HG modes, including their controlled superpositions, can be fabricated with high precision. These considerations establish the HG mode superposition as a viable and experimentally accessible alternative to LG modes for mid-IR OAM generation. This flexibility enables adaptable OAM system design. The R-index thus serves as a fundamental metric for field optimization across the entire electromagnetic spectrum, enabling performance equivalent substitutions.

Critical insights

- **Universal purity quantification:** the R-index enables direct comparison of OAM content across arbitrary fields, from single vortices to complex superpositions, addressing a longstanding gap in structured light characterization.
- **Phase-imprinting performance validation:** by quantifying the beam purity of beams generated by phase manipulation, the R-index provides a tool for optimizing experimental vortex creation methodology. This is particularly crucial for Mid-IR applications where SLMs are unavailable.
- **Design optimization:** the metric identifies LG modes as theoretical optima while revealing HG superpositions as viable alternatives when LG generation is impractical, guiding experimental design choices.

R-index and $\bar{J}_s$ Interpretation

The **R-index** quantifies the fraction of solenoidal currents relative to the net optical current, indicating the percentage of photons in the field that possess OAM. This is useful for quantifying the OAM content relative to other sources of phase gradient/optical current and is therefore a direct measure of how OAM-dominated a beam is. Due to its normalization $0 \leqslant R \leqslant 1$, it is unaffected by the scale parameters of the beam (w_0, k, λ, z_R) and hence can be used as a measure of how perfect the generated beam is, i.e. how close the generated beam is to the ideal OAM-bearing beam profile.

The solenoidal current strength $\bar{J}_s$, in contrast, represents the absolute strength of solenoidal currents. It is useful for assessing the interaction strength. For example, consider two self-similar beams such as LG modes with identical topological charge l, but different waist parameters w_0. Both beams exhibit the same R-index, as their optical current scales equivalently under the corresponding similarity transformation. However, since $\bar{J}_s \propto w_0^{-1}$, the beam with the smaller waist exhibits stronger phase gradients and consequently imparts a higher torque on particles.

For a pure LG beam, the R-index attains a value of 1 at the focal plane, independent of the topological charge. However, as the charge increases, the associated solenoidal energy circulation around the phase singularity becomes more pronounced. When the beam is tightly focused to a smaller waist, the magnitude of the solenoidal current J_s correspondingly increases, whereas an expansion of the beam waist leads to a reduction in J_s. Therefore, the pair $(R, \bar{J}_s)$ provides complementary measures of the relative and absolute value of the OAM content, enabling a more fine-grained differentiation of topological profiles.

7. Analytical calculation of the R-index for LG beams

To analytically corroborate our numerical findings in this section we analytically evaluate the R-index for all LG beams, equation (17), with $p = 0$ and arbitrary l.

The intensity profile of these beams is

$$I(\boldsymbol{r}) = I_0 \left(\frac{w_0}{w(z)}\right)^2 \left(\frac{\sqrt{2}r}{w(z)}\right)^{2|l|} \exp\left(-\frac{2r^2}{w(z)^2}\right), \tag{22}$$

with $I_0 = \frac{c\epsilon_0}{2}|E_0|^2$, and the phase profile reads

$$\varphi = -\frac{kr^2}{2\mathcal{R}(z)} - kz + \xi(z) + l\phi. \tag{23}$$

The phase gradient can be analyzed in simple terms when expressed in cylindrical coordinates

$$\boldsymbol{\nabla}\varphi(\boldsymbol{r}) = \frac{\partial\varphi}{\partial r}\hat{\boldsymbol{r}} + \frac{1}{r}\frac{\partial\varphi}{\partial\phi}\hat{\boldsymbol{\phi}} + \frac{\partial\varphi}{\partial z}\hat{\boldsymbol{z}}. \tag{24}$$

By taking the curl and divergence of each component in the above expression, it is easy to verify that only the azimuthal component is of solenoidal character, $\boldsymbol{f}_R(\boldsymbol{r}) = \frac{l}{r}\hat{\boldsymbol{\phi}}$. The radial component is irrotational, $\boldsymbol{f}_{IR}(\boldsymbol{r}) = -\frac{kr}{\mathcal{R}(z)}\hat{\boldsymbol{r}}$, while the z component does not contribute to $\boldsymbol{f}(\boldsymbol{r}) = \boldsymbol{f}_{IR}(\boldsymbol{r}) + \boldsymbol{f}_R(\boldsymbol{r})$ since $\boldsymbol{f}(\boldsymbol{r})$ lies on the plane perpendicular to the propagation axis $\boldsymbol{z}$, see equation (4).

The R-index of equation (13) can then be calculated analytically by employing the integral [40]

$$\int_0^\infty r^{2k} e^{-\frac{2r^2}{w^2}}\, dr = \frac{(2k)!}{2^{3k+1}k!}\sqrt{\frac{\pi}{2}}w^{2k+1}. \tag{25}$$

Table 4. Same as table 3 but for an extended selection of Hermite–Gaussian superpositions.

SSOF profile	Phase difference	$\bar{J}_s$ units of w_0^{-1}	R-index	Intensity profile
$HG_{3,0} + HG_{0,3}$	$\pi/2$	1.549	0.71	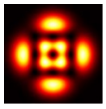
$HG_{3,0} + HG_{0,3}$	$\pi/4$	1.546	0.62	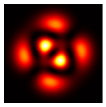
$HG_{1,2} + HG_{2,1}$	$\pi/2$	2.227	0.73	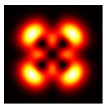
$HG_{1,2} + HG_{2,1}$	$\pi/4$	2.209	0.64	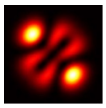
$HG_{1,3} + HG_{3,1}$	$\pi/4$	1.634	0.67	
$HG_{1,3} + HG_{3,1}$	$\pi/3$	1.643	0.75	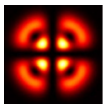
$HG_{2,4} + HG_{4,2}$	$\pi/2$	2.665	0.69	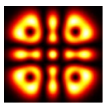
$HG_{2,4} + HG_{4,2}$	$\pi/4$	2.636	0.61	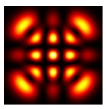
$HG_{2,4} + HG_{4,2}$	$\pi/3$	2.648	0.65	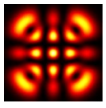
$HG_{3,2} + HG_{2,3}$	$\pi/2$	2.840	0.74	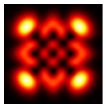
$HG_{3,2} + HG_{2,3}$	$\pi/4$	2.822	0.64	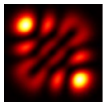
$HG_{3,4} + HG_{4,3}$	$\pi/2$	3.319	0.74	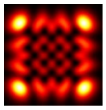

The numerator straightforwardly evaluates to

$$\iint |\boldsymbol{f}_{\mathrm{R}}(\boldsymbol{r})| I(\boldsymbol{r})\, \mathrm{d}A = \sqrt{\frac{\pi^3}{2}} \frac{|l|\,(2|l|)!}{2^{2|l|}|l|!} \frac{I_0 w_0}{\sqrt{1+(z/z_{\mathrm{R}})^2}}. \tag{26}$$

The integral for $|\boldsymbol{f}_{\mathrm{IR}}(\boldsymbol{r})|$ can also be straightforwardly calculated

$$\iint |\boldsymbol{f}_{\mathrm{IR}}(\boldsymbol{r})| I(\boldsymbol{r})\ \mathrm{d}A = \sqrt{\frac{\pi^3}{2}} \frac{(2|l|+2)!}{2^{2|l|+2}\,(|l|+1)!} \frac{I_0 w_0}{\sqrt{1+(z/z_{\mathrm{R}})^2}} \frac{z}{z_{\mathrm{R}}}. \tag{27}$$

Therefore, by using equations (26) and (27) the R-index yields

$$R(z) = \left(1 + \frac{2|l|+1}{2|l|} \frac{z}{z_{\mathrm{R}}}\right)^{-1}. \tag{28}$$

This expression reveals that at the focal plane ($z = 0$) the transverse optical current of a LG beam is purely solenoidal, such that a planar probe detects a purely OAM-bearing flow. As the observation plane moves away from the focus, diffraction-induced radial phase gradients increasingly contribute to the irrotational component, leading to a monotonic decrease of the R-index as the beam diverges. This decrease is more pronounced for low topological charge, e.g. for $l = 1$, $R(z) \simeq 1 - \frac{3}{2} z/z_{\mathrm{R}}$, while for $l \gg 1$ the decay is smoother, approaching $R(z) \simeq 1 - z/z_{\mathrm{R}}$. This scaling independently corroborates the numerical results of table 2 and demonstrates the sensitivity of the R-index to low-l OAM states.

Importantly, the reduction of R with propagation does not indicate a loss of OAM, which remains conserved under free-space propagation, but rather a decrease in the fraction of transverse optical current that circulates azimuthally on a given plane. The R-index therefore quantifies the locally accessible intrinsic OAM relevant for planar light–matter interactions and should be evaluated at the interaction plane. Its propagation dependence is thus an essential feature, capturing how effectively OAM can be accessed in realistic experimental geometries.

8. Conclusion

In this work, we introduced the R-index, a robust metric to quantify the intrinsic OAM content of SSOFs. It establishes a unified framework for quantifying intrinsic OAM content. By directly measuring the relative intensity-weighted solenoidal energy, the R-index provides a quantitative assessment of mode purity and the fraction of photons available for OAM-mediated interactions, even in complex fields with multiple vortices.

Unlike traditional approaches based on vortex counting or modal decomposition, the R-index decouples beam purity from topological charge and provides a quantitative measure of mode purity. It offers a robust tool for enabling empirical optimization of OAM sources. Our calculations demonstrate its applicability across a range of beam types, including LG, Gaussian, spiral phase plate-generated, and HG beams, making it a universal tool for structured light analysis. To our knowledge, this is the first demonstration of a universal OAM quantification method based on a single index, enabling direct comparison of disparate field structures, including LG beams and complex multi-vortex superpositions, on an equal footing. This facilitates the identification of the most OAM-efficient configuration, regardless of field complexity. Future directions include extending the R-index framework to vectorial fields, experimental validation through interferometry or modal decomposition, and exploring its behavior under beam propagation or turbulence.

Data availability statement

The code and instructions to reproduce the data and analyses are available at: https://github.com/SFB-Comb-at-P2-P3-Collaboration/R-indices. The data underlying the figures/tables are generated by the provided workflow; outputs can be reproduced by running the code as described.

Acknowledgments

This research was funded in whole or in part by the Austrian Science Fund (FWF) [10.55776/F1004]. For open access purposes, the author has applied a CC BY public copyright license to any author accepted manuscript version arising from this submission.

Author contributions

Mikhail Maslov 0000-0003-4074-2570
Writing – review & editing (supporting)

Tom Jungnickel
Writing – review & editing (supporting)

Timo Gaßen
Writing – review & editing (supporting)

Mikhail Lemeshko 0000-0002-6990-7802
Project administration (supporting), Supervision (supporting)

Appendix. Solenoidal phase gradient magnitudes and R-index values for various SSOFs

This appendix includes the table 4 providing an extensive array of examples of SSOFs with their associated $\bar{J}_s$ and R-index values.

References

[1] Allen L, Beijersbergen M W, Spreeuw R J C and Woerdman J P 1992 Orbital angular momentum of light and the transformation of Laguerre-Gaussian laser modes *Phys. Rev. A* **45** 8185–9
[2] Willner A E *et al* 2015 Optical communications using orbital angular momentum beams *Adv. Opt. Photonics* **7** 66–106
[3] Yao A M and Padgett M J 2011 Orbital angular momentum: origins, behavior and applications *Adv. Opt. Photonics* **3** 161–204
[4] Yang C, Liu R, Ni W, Wang S, Tian Y, Hou J, Chen S and Shum P P 2023 High-order oam states unwrapping in multiplexed optical links *APL Photonics* **8** 056110
[5] He H, Friese M E J, Heckenberg N R and Rubinsztein-Dunlop H 1995 Direct observation of transfer of angular momentum to absorptive particles from a laser beam with a phase singularity *Phys. Rev. Lett.* **75** 826–9
[6] Volpe G *et al* 2023 Roadmap for optical tweezers *J. Phys. Photon.* **5** 022501
[7] Maslov M, Koutentakis G M, Hrast M, Heckl O H and Lemeshko M 2024 Theory of angular momentum transfer from light to molecules *Phys. Rev. Res.* **6** 033277
[8] Ruchi, Senthilkumaran P and Pal S K 2020 Phase singularities to polarization singularities *Int. J. Opt.* **2020** 2812803
[9] Senthilkumaran P 2024 *Singularities in Physics and Engineering: Properties, Methods and Applications (IOP Series in Advances in Optics, Photonics and Optoelectronics)* 2nd edn (Institute of Physics Publishing)
[10] Awasthi S and Kang S 2022 Generation of few μm high optical vortex using tunable spiral plates *J. Phys. Photon.* **4** 034001
[11] Rosales-Guzmán C, Perez-Garcia B and Cox M A 2024 The compact cookbook of structured modes of light *J. Phys. Photon.* **6** 043004
[12] Yang D, Sun D, Feng J, Yang Z, Zhou K, Wang L, Lin J and Jin P 2024 Generation of dynamic rotation propagation vortex beam by a Fibonacci series annular subzone vortex phase *J. Phys. D: Appl. Phys.* **57** 295101
[13] Andrews D, Romero L and Babiker M 2004 On optical vortex interactions with chiral matter *Opt. Commun.* **237** 133–9
[14] Babiker M, Bennett C R, Andrews D L and Dávila Romero L C 2002 Orbital angular momentum exchange in the interaction of twisted light with molecules *Phys. Rev. Lett.* **89** 143601
[15] D L Andrews and M Babiker 2012 *The Angular Momentum of Light* (Cambridge University Press)
[16] Forbes K A and Andrews D L 2021 Orbital angular momentum of twisted light: chirality and optical activity *J. Phys. Photon.* **3** 022007
[17] Zhou Z Y, Li Y, Ding D S, Shi B S and Guo G C 2016 Orbital angular momentum photonic quantum interface *Light Sci. Appl.* **5** e16019
[18] Molina-Terriza G, Torres J P and Torner L 2007 Twisted photons *Nat. Phys.* **3** 305–10
[19] Forbes K A 2019 Raman optical activity using twisted photons *Phys. Rev. Lett.* **122** 103201
[20] Lloyd S M, Babiker M and Yuan J 2012 Interaction of electron vortices and optical vortices with matter and processes of orbital angular momentum exchange *Phys. Rev. A* **86** 023816
[21] Schmiegelow C, Schulz J, Kaufmann H, Ruster T, Poschinger U and Schmidt-Kaler F 2016 Transfer of optical orbital angular momentum to a bound electron *Nat. Commun.* **7** 12998
[22] Bliokh K Y and Nori F 2015 Transverse and longitudinal angular momenta of light *Phys. Rep.* **592** 1–38
[23] Bekshaev A, Bliokh K Y and Soskin M 2011 Internal flows and energy circulation in light beams *J. Opt.* **13** 053001
[24] Kotlyar V V and Kovalev A A 2021 Optical vortex beams with a symmetric and almost symmetric oam spectrum *J. Opt. Soc. Am. A* **38** 1276–83
[25] Berry M V 2009 Optical currents *J. Opt. A: Pure Appl. Opt.* **11** 094001
[26] McDonald K 2015 Orbital and spin angular momentum of electromagnetic fields (available at: https://api.semanticscholar.org/CorpusID:2855874)
[27] Born M, Wolf E, Bhatia A B, Clemmow P C, Gabor D, Stokes A R, Taylor A M, Wayman P A and Wilcock W L 1999 *Principles of Optics: Electromagnetic Theory of Propagation, Interference and Diffraction of Light* 7th edn (Cambridge University Press)
[28] Bahl M and Senthilkumaran P 2012 Helmholtz hodge decomposition of scalar optical fields *J. Opt. Soc. Am. A* **29** 2421–7
[29] Ku J and Reichel L 2020 A novel iterative method for discrete helmholtz decomposition *Appl. Numer. Math.* **151** 161–71
[30] Suda T 2020 Application of Helmholtz-Hodge decomposition to the study of certain vector fields *J. Phys. A: Math. Theor.* **53** 375703
[31] Light J C and Carrington Jr. T 2000 *Discrete-Variable Representations and Their Utilization* (Wiley) pp 263–310
[32] Schumann U and Sweet R A 1988 Fast Fourier transforms for direct solution of Poisson's equation with staggered boundary conditions *J. Comp. Phys.* **75** 123–37
[33] Yang J, Wang Z, Song J, Lv R, Wang X, Zhu J and Wei Z 2021 Diode-pumped 10 W femtosecond Yb:CALGO laser with high beam quality *High Power Laser Sci. Eng.* **9** e33
[34] Yang Y, Li D, Zhang Y, Li P, Wu Y, Yan P, Gong M and Xiao Q 2025 3 kW narrow-linewidth linearly polarized fiber laser with high-purity single-mode output and high PER enabled by suppressing mode and polarization coupling *Opt. Laser Technol.* **186** 112729
[35] Sueda K, Miyaji G, Miyanaga N and Nakatsuka M 2004 Laguerre-Gaussian beam generated with a multilevel spiral phase plate for high intensity laser pulses *Opt. Express* **12** 3548–53
[36] Karimi E, Zito G, Piccirillo B, Marrucci L and Santamato E 2007 Hypergeometric-Gaussian modes *Opt. Lett.* **32** 3053–5
[37] Andersen J M, Alperin S N, Voitiv A A, Holtzmann W G, Gopinath J T and Siemens M E 2019 Characterizing vortex beams from a spatial light modulator with collinear phase-shifting holography *Appl. Opt.* **58** 404–9
[38] Ohtomo T, Chu S-C and Otsuka K 2008 Generation of vortex beams from lasers with controlled Hermite- and Ince-Gaussian modes *Opt. Express* **16** 5082–94
[39] Chu S-C, Chen Y-T, Tsai K-F and Otsuka K 2012 Generation of high-order Hermite-Gaussian modes in end-pumped solid-state lasers for square vortex array laser beam generation *Opt. Express* **20** 7128–41
[40] Zwillinger D, Moll V, Gradshteyn I and Ryzhik I 2014 *Table of Integrals, Series and Products (Eighth Edition)* 8th edn (Academic)